Published in final edited form as:

Int J Radiat Oncol Biol Phys. 2021 June 01; 110(2): 551–565. doi:10.1016/j.ijrobp.2020.12.028.

Small Animal IMRT Using 3D-Printed Compensators

Gage Redler, PhD[*], **Erik Pearson, PhD**[†], **Xinmin Liu, PhD**[†], **Inna Gertsenshteyn, BA**[†], **Boris Epel, PhD**[†], **Charles Pelizzari, PhD**[†], **Bulent Aydogan, PhD**[†], **Ralph Weichselbaum, MD**[†], **Howard J. Halpern, MD, PhD**[#†], **Rodney D. Wiersma, PhD**[#‡]

[*]Moffitt Cancer Center, Department of Radiation Oncology, Tampa, Florida;

[†]Department of Radiation and Cellular Oncology, University of Chicago, Chicago, Illinois;

[‡]Department of Radiation Oncology, University of Pennsylvania, Philadelphia, Pennsylvania

[#] These authors contributed equally to this work.

Abstract

Purpose: Preclinical radiation replicating clinical intensity modulated radiation therapy (IMRT) techniques can provide data translatable to clinical practice. For this work, treatment plans were created for oxygen-guided dose-painting in small animals using inverse-planned IMRT. Spatially varying beam intensities were achieved using 3-dimensional (3D)-printed compensators.

Methods and Materials: Optimized beam fluence from arbitrary gantry angles was determined using a verified model of the XRAD225Cx treatment beam. Compensators were 3D-printed with varied thickness to provide desired attenuation using copper/polylactic-acid. Spatial resolution capabilities were investigated using printed test-patterns. Following American Association of Physicists in Medicine TG119, a 5-beam IMRT plan was created for a miniaturized (~1/8th scale) C-shape target. Electron paramagnetic resonance imaging of murine tumor oxygenation guided simultaneous integrated boost (SIB) plans conformally treating tumor to a base dose (Rx_1) with boost (Rx_2) based on tumor oxygenation. The 3D-printed compensator intensity modulation accuracy and precision was evaluated by individually delivering each field to a phantom containing radiochromic film and subsequent per-field gamma analysis. The methodology was validated end-to-end with composite delivery (incorporating 3D-printed tungsten/polylactic-acid beam trimmers to reduce out-of-field leakage) of the oxygen-guided SIB plan to a phantom containing film and subsequent gamma analysis.

Corresponding author: Gage Redler, PhD; Gage.Redler@moffitt.org.

Disclosures: B.E. and H.J.H. disclose financial interest in O2M Technologies, LLC. R.W. has a patent “Methods and Kits for Diagnosis and Triage of Patients With Colorectal Liver Metastases” pending. H.J.H. has a patent “Magnetic Resonance Analysis of Substances in Samples that Include Dissipative Material” (No. 4,714,886) issued, a patent “Selective Isotopic Labelling of Spin Labels for Electron Resonance Spectroscopy” (No. 5,431,901) issued, a patent “Imaging System Performing Substantially Exact Reconstruction and Using Nontraditional Trajectories” (No. 7,444,011) issued, a patent “High Isolation Transmit/Receive Surface Coils and Method for EPRI” (No. 8,644,955 B1) issued, a patent “T1-Senstive Inversion-Recovery-Imaging Method and Apparatus for EPRI” (No. 9,392,957 B1) issued, and a patent “Method and Apparatus for Resonator Signal Production and Measurement” (No. 10,551,450 B2) issued.

Data sharing statement: Research data are stored in an institutional repository and will be shared upon request to the corresponding author.

Supplementary material for this article can be found at https://doi.org/10.1016/j.ijrobp.2020.12.028.

Results: Resolution test-patterns demonstrate practical printer resolution of ~0.7 mm, corresponding to 1.0 mm bixels at the isocenter. The miniaturized C-shape plan provides planning target volume coverage ($V_{95\%}$ = 95%) with organ sparing (organs at risk D_{max} < 50%). The SIB plan to hypoxic tumor demonstrates the utility of this approach (hypoxic tumor $V_{95\%,Rx2}$ = 91.6%, normoxic tumor $V_{95\%,Rx1}$ = 95.7%, normal tissue $V_{100\%,Rx1}$ = 7.1%). The more challenging SIB plan to boost the normoxic tumor rim achieved normoxic tumor $V_{95\%,Rx2}$ = 90.9%, hypoxic tumor $V_{95\%,Rx1}$ = 62.7%, and normal tissue $V_{100\%,Rx2}$ = 5.3%. Average per-field gamma passing rates using 3%/1.0 mm, 3%/0.7 mm, and 3%/0.5 mm criteria were 98.8% ± 2.8%, 96.6% ± 4.1%, and 90.6% ± 5.9%, respectively. Composite delivery of the hypoxia boost plan and gamma analysis (3%/1 mm) gave passing results of 95.3% and 98.1% for the 2 measured orthogonal dose planes.

Conclusions: This simple and cost-effective approach using 3D-printed compensators for small-animal IMRT provides a methodology enabling preclinical studies that can be readily translated into the clinic. The presented oxygen-guided dose-painting demonstrates that this methodology will facilitate studies driving much needed biologic personalization of radiation therapy for improvements in patient outcomes.

Introduction

Radiation therapy (RT) is an essential component to successful cancer treatment and management, along with surgery and chemotherapy. There have been steady gains in 5-year survival rates for patients with cancer, attributed in part to technological advancements allowing better targeting of radiation to diseased tissue.[1] In recent decades, RT technology has developed dramatically, with intensity modulated RT (IMRT) representing one of the most significant developments. Rather than conforming uniform intensity beams to 3-dimensional (3D) objects, varying beam intensity across each conformal aperture provides additional degrees of freedom. Patient-specific beam compensators with spatially varying thicknesses tailor beam intensity and thus dose distribution to patient anatomy. Eventually, multileaf collimators (MLCs) provided flexibility to shape and modulate radiation fields and replaced compensators. IMRT facilitated more effective treatment methodologies, including simultaneous integrated boosts (SIBs) to higher-risk and/or radioresistant tumor regions or even image guided dose painting based on biologic and physiological characteristics.[2,3]

Although crucial to the success of modern RT, these developments have been technology driven. Further advances will come from using these technological advances to pursue biology- driven developments. Before clinical implementation, preclinical techniques analogous to modern clinical techniques are needed to investigate various approaches. Cancer biology research guiding clinical treatment often requires preliminary studies on the cellular or small animal scale.[4–6] However, the fundamental difference between technologies and methodologies in these preliminary studies versus in the clinic hinders translation. Specifically, preclinical studies often use bulk irradiation delivering a single dose to an entire cell culture or animal tumor/body section. Irradiator calibration, dose calculation, and radiation delivery approaches are often imprecise or irreproducible.[7] Even meticulous preclinical studies struggle to translate to the clinic due to fundamental differences in methodologies.[8] Differences include relative biological effectiveness between megavoltage clinical beams and kilovoltage (kV) preclinical beams,[9] biologically effective dose due to

varied fractionation,[10] nonconformal and inhomogeneous doses prescribed to a single point and/or irradiation often with a single field in preclinical studies versus highly conformal homogeneous treatments prescribed using 3D isodose distributions and irradiation with multiple beam angles in clinical studies,[11,12] and a general lack of precision preclinically that is provided via image guidance, immobilization, and motion management in the clinical setting.[7]

The importance of standardizing preclinical radiation studies using clinically analogous methodologies has recently come to the forefront with the development of image guided, precision small animal irradiators. This is evidenced by the recent report commissioned by the European Society for Radiotherapy and Oncology Advisory Committee in Radiation Oncology Practice, which reviewed the state of technology and issued recommendations for "this new field of research."[7] Preclinical irradiator technologies have been reviewed in the literature.[7,9]

Beam collimation for these irradiators is generally accomplished using interchangeable fixed-aperture inserts (or in some cases motorized adjustable apertures).[13–17] These improve conformality versus large-field bulk-irradiators, but they only shape the beam (usually in simple geometric shapes) and do not modulate intensity. Adapting clinical MLC systems to the preclinical scale has been virtually impossible with current technology.[18] Alternatives to miniaturized MLCs are under development and include rastered pencil beams,[19] carbon nanotube field emission cathodes,[20–22] and sparse orthogonal collimators.[23,24] A comprehensive summary of various approaches to scaling MLCs and other collimators to the preclinical scale can be found in the publication by Woods et al.[24] Each solution has its own particular pros and cons, but in general, the approach presented in this work seeks to address or avoid issues such as complex, costly engineering or equipment, prohibitively long treatments, moving parts and electronics requiring quality control, and limited spatial resolution. Furthermore, there are currently no widely available treatment planning systems for IMRT with these preclinical irradiators, which require optimization-based inverse planning to determine optimal fluences from multiple beam angles producing the desired 3D dose distribution.

This work presents a preclinical IMRT methodology modeled after clinical IMRT, which relies on an inverse planning dose calculation engine to determine optimal bixel (discretized subsections of beam aperture) intensities. These are converted into copper-doped polylactic acid (CuPLA) plastic thicknesses producing appropriate beam attenuation, which are 3D printed and mounted in front of the open beam. Recently, there has been growing interest in the concept of using modern 3D printing technology for such applications. The method presented herein uses high-Z printing material to directly print positive blocks. Alternative approaches have been presented that print negative block molds that can then be filled with high-Z material.[25] These differing approaches have different drawbacks and benefits, but in general they represent a growing novel means of implementing clinically analogous IMRT on the preclinical scale.

The capability of the presented approach was demonstrated on a miniaturized C-shape target and cylindrical organ-at-risk (OAR) core from the test suite of mock clinical cases for IMRT

planning provided by American Association of Physicists in Medicine.[26] The utility was then demonstrated via 2 SIB IMRT plans treating a murine tumor while selectively increasing radiation dose to the hypoxic or (representing a control) the normoxic sub-volume of a murine tumor, as delineated by oxygen imaging with electron paramagnetic resonance imaging (EPRI).[27–30] This example was chosen because the role of hypoxia in cancer illustrates why translatable preclinical radiation methodologies are needed. For over a century,[31] studies have shown the importance of hypoxia in radiation response,[32–35] but tumor oxygenation status has mostly failed to translate clinically. Oxygen imaging could be incorporated into treatment planning, but preclinical tools to study how to accomplish this are still needed.[27] Low levels of tumor oxygenation (hypoxia) is an example for potential local regions of increased tumor resistance. This issue applies to a myriad of functional imaging modalities and parameters affecting treatment efficacy that have yet to translate from preclinical studies to clinical improvements. This work addresses the challenge of adapting technologies from clinical treatments down to preclinical scale to aid in these efforts.

Methods and Materials

Treatment planning

To enable IMRT planning, a model of the treatment beam was generated; specifically, photon fluence for the XRAD225Cx (Precision X-Ray, North Branford, CT) used in this work.[13] This allows propagation of this beam through arbitrary irradiated objects, which is necessary for calculation of delivered dose distributions. This work used the open-source matRad software as the dose calculation engine.[36] The matRad pencil beam dose algorithm was commissioned following the method of Bortfield et al,[37] focusing on accuracy in the kilovoltage energy range. Monte Carlo (BEAMnrc/EGSnrc, specifically DOS-XYZnrc[38]) simulation-generated primary/scatter doses in water were used for circular beams of various diameters. Curve fitting was performed in Matlab (Mathworks, Natick, MA) to generate matRad beam model parameters. Validation included a comparison of calculated and measured (solid water phantom, EBT3 gafchromic film) lateral and depth dose profiles. Details on beam commissioning for similar applications are available elsewhere.[7,39]

In this work, 5 equally spaced coplanar gantry angles were used. The discretized bixel intensities from each angle were the variables optimized during IMRT planning, which were converted to compensator thicknesses. The optimizer cost function is a piecewise quadratic, incorporating over- and underdose and uniformity penalties. The assigned weight to over- and underdose penalty provides flexibility to balance dosimetric goals (eg, to simultaneously pursue target coverage and limit hotspots or to simultaneously increase dose to target and decrease dose to abutting OAR). The upper and lower bounds of bixel intensity were defined based on the limitations of minimum and maximum compensator thicknesses (see the next section). Following clinical IMRT paradigms, desired dose distributions are based on dose-volume histograms (DVHs) and specified dose-volume criteria (eg, coverage of target by certain doses and limits on nearby normal tissue volume receiving certain doses). Specifically, tumor goals were $D_{95\%} \geq 100\%$, $V_{110\%} \leq 10\%$; the oxygen-guided boost region goal was $D_{95\%} \geq 158\%$; and the OAR/normal tissue goal was $V_{50\%} \leq 5\%$.

Compensator generation

We used 3D-printed compensators to modulate the uniform-intensity XRAD225Cx beam to produce optimized bixel intensities. The compensator material was MetalFil (Formfutura BV, Nijmegen, Netherlands) metal-doped plastic filament consisting of 80% copper, 20% PLA (CuPLA). Compensators were printed with a MakerGear M3-ID fused deposition model 3D printer (MakerGear, LLC, Beachwood, OH). The linear attenuation coefficient (μ) of CuPLA was measured for our 225 kVp treatment beam to be 0.19 mm^{-1}. Compensator thickness, t, for given bixel intensity, I_b, was calculated from the Beer-Lambert law, $I_b = I_0 e^{(-\mu t)}$, where I_o is unmodulated intensity.

Compensators were modeled as stepped cylindrical plugs with a positive orientation feature designed to fit into a custom (3D-printed) collimator mount in the XRAD225Cx system (see Fig. 4d,e later in the text, for examples of the described shape). A compensator thickness map was generated as a group of rectangular prisms with in-plane location and dimensions corresponding to bixel location and dimensions (back projected from isocenter; 307 mm from source) to the compensator location (200 mm from source) and height corresponding to optimized thickness. This was inverted and removed from the 20-mm thick cylindrical plug for the customized beam compensator 3D model. Slicer software (Simplify3D, Cincinnati, OH) generated the 3D printer gcode. Print settings included extrusion multiplier 1.0, extrusion width 0.25 mm (smaller than 0.35 mm physical nozzle to retain fine features after slicing), layer thickness 0.2 mm, infill 100% with 10° rotation for each subsequent layer. Although the dosimetric effect was suspected to be minimal, the 10° layer rotation was used instead of the default crisscross approach provided by a 90° rotation to avoid internal gaps and patterned print heterogeneity consistent in the plane perpendicular to the beam axis that could sum together throughout the compensator.

Minimum and maximum compensator thicknesses were constrained (0.4 and 20.0 mm, respectively) to provide structural support at the compensator base and avoid impractical thicknesses (to both reduce required printing material and minimize the influence of beam divergence, which is not modelled in this current iteration and increases with compensator thickness), respectively. Bixel size was limited by fused deposition model printing mechanics. The finite deposited layer thickness (0.2 mm) governs the discretization of compensator thickness and bixel intensity. In-plane bixel size is governed by 3D printer in-plane resolution. Radiographs of CuPLA printed structures with 0.5-, 0.7-, and 1.0-mm grid spacings tested resolution limitations (Fig. 1).

To reduce unwanted out-of-field dose leakage in fully blocked portions of the beam, a more highly attenuating tungsten-doped PLA (WPLA), consisting of 92% to 95% metal, was used to produce field trimmers (Rapid 3DShield Tungsten Filament; The Virtual Foundry, Stoughton, WI). The addition of a 5-mm thick WPLA layer for the blocked portion of the field outside of the region with intensity modulated by the CuPLA compensator was found to reduce out-of-field transmission to ~3% (comparable to clinical MLC transmission). These trimmers are only used for composite delivery from all 5 planned fields (not individual field delivery and analysis) where the low-dose leakage from each field compounds to create larger discrepancies.

Dose measurement and analysis

The ability to deliver highly modulated dose distributions was tested using analogs to clinical, patient-specific quality assurance (QA) methods. Each beam from the IMRT plans was individually cast onto a QA phantom and the dose distribution was recalculated. Planned dose planes (central plane of the phantom perpendicular to the axis of the treatment beam) were extracted and compared with measurements. The QA phantom was a split 20 × 20 × 20 mm^3 acrylic cube that held a laser-cut 20 × 20 mm^2 piece of EBT3 gafchromic film in the central plane (Fig. 2). The phantom was aligned with the computed tomography (CT) system of the XRAD225Cx and indexed to the support platform for repeat positioning. A film sensitometric curve was generated by delivering known doses to film, thereby correlating optical density to dose.[40]

In addition to per-field measurements, composite dose from complete end-to-end delivery of all 5 IMRT fields for the hypoxia boost (SIB) plan was analyzed. These fields were all cast onto the acrylic cube QA phantom, and recalculated dose was extracted for the central axial (plane of gantry rotation) and coronal (plane perpendicular to beam axis with gantry at 0°) planes. This planned dose was measured twice with film oriented in the corresponding planes of the QA phantom.

Fidelity of delivered to planned dose was assessed using per-field and composite dose 2-dimensional (2D) planar gamma analysis.[41] Common clinical parameters were adjusted for preclinical scale: 3%/1.0 mm, 3%/0.7 mm, 3%/0.5 mm for per-field analysis and 3%/1.0 mm for composite dose analysis (15% low dose threshold). Film calibration and gamma analysis were done with RIT software (Radiologic Imaging Technology, Inc, Colorado Springs, CO).

Planning cases

American Association of Physicists in Medicine TG119 provides a suite of planning cases for testing clinical IMRT systems.[26] The C-shape target (planning target volume) with central avoidance structure (OAR) was scaled down to ~1/8th size to represent preclinical scale (Fig. 3a). Note that a young adult female C3H mouse has a mass of ~20 g and a Sprague-Dawley female rat is ~300 g. Our scaling, therefore, approximates the root-mean-square linear scale reduction from the classic 70 kg human to preclinical subjects, which is ~1/9th. Dimensions were avoidance core radius r=1.2 mm; avoidance core length l=13.2 mm; target inner r=2.0 mm; outer radius r=4.8 mm; and 0.8 mm separation between avoidance and target (compared with clinical dimensions of 10.0, 100.0, 15.0, 37.0, and 5.0 mm, respectively). A fixed-field 5-beam IMRT plan was created with the goal of uniformly covering the target with prescription dose (100%) while limiting OAR maximum dose to <50%.

Retrospective mouse data were used to plan murine tumor (FSa fibrosarcoma xenograft subcutaneously implanted on hind limb) treatments with EPRI-identified hypoxic region SIB. This consisted of a CT (XRAD225Cx on-board imager, Fig. 3d), T2-weighted magnetic resonance imaging (MRI) (9.4T preclinical system, not shown), and EPRI oxygen image (Fig. 3g). These images were registered.[42] MRI delineated tumor from normal tissue. CT segmented the remaining anatomy and provided density for dose calculation. EPRI

provided the location of hypoxia ($pO_2 \leq 10$ torr). Figure 3d shows these regions delineated on the CT. Previously determined 15% and 95% tumor control doses ($TCD_{15\%}/TCD_{95\%}$) of 22.5 Gy and 35.5 Gy[27] were the basis for SIB prescriptions of $Rx_1 = TCD_{15\%} = 22.5$ Gy to the normoxic tumor, while boosting hypoxic tumor to $Rx_2 = TCD_{95\%} = 1.58 \cdot Rx_1 = 35.5$ Gy. Additionally, dose to normal tissue was minimized. To illustrate flexibility, an inverted-boost plan was generated to instead deliver Rx_1 to hypoxic tumor and Rx_2 to normoxic tumor, while minimizing dose to normal tissue (ie, representing a control plan in a randomized co-clinical trial).

Results

3D-printed compensator resolution

Figure 1d–f shows images of 3D-printed resolution test patterns with edges separated by 0.5, 0.7, and 1.0 mm. Figure 1g shows intensity profiles across images of these test patterns (arbitrarily offset in vertical axis for visualization of features). Practical bixel size was determined to be ~0.7 mm, based on ability to resolve discrete regions in the 0.7 mm but not 0.5 mm resolution patterns. This limitation is for physical print size, which, when projected to isocenter, corresponds to the bixel size of 1.0 mm used.

3D-printed compensator IMRT plans

Figure 3 shows planning capabilities of the 3D-printed compensator IMRT methodology. Figure 3a–c shows a central slice of the CT (in gantry-rotation plane) for the miniaturized C-shape target, planned dose distribution (in gantry-rotation plane) for the optimized 5-field IMRT plan, and corresponding DVH, respectively. The utility of IMRT is apparent in the dose distribution conformality/concavity and steep dose gradients between target and OAR. This is further illustrated in the DVH showing impressive planning target volume coverage ($V_{95\%} = 95\% \cdot Rx$) with simultaneous normal tissue sparing (OAR $D_{max} < 50\% \cdot Rx$). Using DVH parameters during planning is analogous to clinical treatment planning and provides robust evaluation of preclinical IMRT plans.

Figure 3d shows a central slice (in gantry-rotation plane) of the mouse fibrosarcoma-bearing hind leg CT with superimposed tumor contour, defined from the T2 MRI (not shown) and the hypoxic tumor subvolume, defined from the EPR pO_2 image (Fig. 3g). Resulting contours of the different regions (hypoxic tumor, normoxic tumor, normal tissue) are in Figure 3d. Associated dose distribution in the same plane of the hypoxic boost 5-field IMRT and DVH for this plan are in Figure 3e and 3f, respectively. IMRT is necessary to produce multiple conformal dose levels in different tumor subregions, enabling SIB treatment. This is emphasized in the DVH, which shows coverage of hypoxic tumor by the high-dose prescription ($V_{95\%,Rx_2} = 91.6\%$), coverage of normoxic tumor by the low-dose prescription ($V_{95\%,Rx_1} = 95.7\%$), and sparing of surrounding normal tissue ($V_{100\%,Rx_1} = 7.1\%$).

The robustness of this approach is further demonstrated in Figure 3h,i, showing associated dose distribution in the same plane as Figure 3d,e,g, but for an inverted-boost delivering Rx_2 to normoxic tumor and Rx_1 to hypoxic tumor. Figure 3e and 3h show this inversion of high and low prescription dose regions. The ability to deliver high dose to a rim region while

decreasing dose to the core region (Fig. 3h) is provided by IMRT. The DVH in Figure 3i shows the normoxic rim is well covered by the high-dose prescription ($V_{95\%,Rx_2} = 90.9\%$), the hypoxic central region is moderately covered by the low-dose prescription, the amount of high dose received is limited ($V_{100\%,Rx_1} = 55\%$, $V_{95\%,Rx_1} = 62.7\%$, $V_{80\%,Rx_1} = 82.3\%$, $V_{100\%,Rx_2} = 0.0\%$), and surrounding normal tissue receiving high dose is limited ($V_{100\%,Rx_2} = 5.3\%$, $V_{100\%,Rx_1} = 48.4\%$).

The most time-consuming parts of the treatment planning are dose matrix calculation and subsequent dose optimization. In these examples, using 5 evenly distributed beams with 1.0-mm bixels and a dose matrix with 0.3-mm elements ($67 \times 67 \times 67$ voxels^3), dose matrix calculation took ~40 seconds and dose optimization took 15 to 30 seconds (using an i7 processor with 3.30 GHz and 64 GB of RAM).

The process for arriving at these treatment plans and converting them into 3D-printed compensator-based deliverable IMRT plans is depicted in Figure 4 for the 5-field IMRT hypoxia-boost plan. The gantry angles and optimized bixel intensities for each are shown as the inner 2D planar maps in Figure 4a. The corresponding conversion of these intensities to compensator thicknesses is shown in the outer 2D planar maps in Figure 4a. An example of 1 optimized bixel intensity map, using 1.0-mm bixels (defined at isocenter) is in Figure 4b. Conversion into 3D-printed compensator thicknesses (geometrically scaled based on beam divergence to 0.7-mm bixels at the compensator plane) is in Figure 4c. Placement of this thickness map within a standard compensator plug and conversion to a sliced 3D-printer compatible model is in Figure 4d. The final 3D-printed compensator using CuPLA is in Figure 4e (printing took ~30 minutes per compensator; 25% time increase with trimmers included). Finally, the result of delivering this intensity modulated field to the acrylic cube QA phantom containing gafchromic film is in Figure 4f, with darker film regions corresponding to higher doses.

Plan deliverability—individual fields

An analogous approach to clinical patient-specific QA for verifying IMRT planned to delivered dose fidelity via per-field planar gamma analysis demonstrates plan deliverability. The acrylic phantom containing gafchromic film was aligned with the film plane at isocenter and perpendicular to the beam axis with gantry at 0° (Fig. 2). Each compensator was mounted in turn and individually delivered to the separate films within the phantom. Dose at this plane within the phantom was calculated separately for each beam delivery for comparison. Qualitative analysis of the dose distribution features can be made as well as quantitative analysis via the gamma criterion.

Figure 5 shows this analysis for a sample field from the miniaturized C-shape target. Qualitative analysis shows similarity in features of the planar doses (planned and delivered in Fig. 5a and b, respectively) as well as similarity in features of the dose profiles (thresholded at 15% of D_{max}) in Figure 5c and d (horizontal and vertical profiles, respectively, corresponding to lines in Fig. 5a and b). Dose falloff outside of the target is well reproduced, as well as the steep gradient needed to spare the central OAR. Gamma

analysis results are shown in Figure 5e–g. Planned planar dose is displayed in grayscale (white regions are below 15% threshold) and points failing gamma analysis are in red for criteria of 3%/1.0 mm, 3%/0.7 mm, and 3%/0.5 mm in Figure 5e, 5f, and 5g, respectively. Similar analysis was performed for all 5 IMRT field planar dose distributions, which resulted in average gamma passing rates of 97.4% ± 4.6%, 93.6% ± 4.3%, and 90.4% ± 4.6% for criteria of 3%/1.0 mm, 3%/0.7 mm, and 3%/0.5 mm, respectively.

Figure 6 shows this analysis for a sample field from the hypoxia-boost plan. Qualitative analysis comparing planned (Fig. 6a) and delivered (Fig. 6b) planar dose and associated dose profiles (Fig. 6c,d) demonstrates the ability of the 3D-printed compensator-based IMRT approach to faithfully produce complex beam fluence patterns with steep intensity gradients. The gamma analysis in Figure 6e–g provides a quantitative demonstration. Average gamma passing rates for all 5 fields were 99.1% ± 1.4%, 96.9% ± 4.4%, and 87.5% ± 8.4% for gamma criteria of 3%/1.0 mm, 3%/0.7 mm, and 3%/0.5 mm, respectively. The inverted-boost plan was similarly analyzed with average gamma passing rates of 99.8% ± 0.3%, 99.3% ± 0.5%, and 94.0% ± 1.6% for criteria of 3%/1.0 mm, 3%/0.7 mm, and 3%/0.5 mm, respectively. Average gamma passing rates, for criteria of 3%/1.0 mm, 3%/0.7 mm, and 3%/0.5 mm, over all 3 IMRT plans (miniaturized C-shape, hypoxia boost, inverted boost; 15 total fields) were 98.8% ± 2.8%, 96.6% ± 4.1%, and 90.6% ± 5.9%, respectively.

Plan deliverability—composite dose

For each individual field, the gamma passing rates show that the CuPLA 3D-printed compensators produce the desired intensity modulation. However, there is significant out-of-field leakage through the fully blocked (20 mm CuPLA) portion of the field. When delivering all treatment fields for an end-to-end composite dose validation, this unwanted low-dose leakage compounds and significantly reduces fidelity of delivered to planned dose distribution. This leakage can be seen in the low-dose background present in Figures 5b and 6b. This is shown in more detail in the supplemental figures. Figure E1 compares individual field deliveries with and without WPLA trimmers. Figure E2 shows composite delivery without WPLA trimmers. Dose profile comparison (Fig. E2c,d) shows a large discrepancy in the low-dose tails. Figure E2e shows that gamma passing rates for 3%/1 mm (15% threshold) criterion are very poor (30.8%) but that these failing points are predominantly outside of the 50% isodose lines and therefore mostly due to the out-of-field leakage dose (Fig. E2f shows gamma passing increases to 81.9% with a 50% threshold applied).

For this proof-of-concept work, additional WPLA field trimmers were printed for the composite plan delivery to reduce this leakage (from ~13% of maximum field dose to ~3%; see Fig. E1). Figure 7 shows the result of the end-to-end test using these trimmed compensators for the hypoxia boost plan. Here, all 5 IMRT fields were delivered from their respective gantry angles to the QA phantom with the film oriented in both the axial (plane of gantry rotation) and coronal (plane perpendicular to gantry 0° axis) planes. Gamma analysis of these 2 dose planes used criterion of 3%/1 mm (15% threshold) pass at a rate of 95.3% and 98.1% for the axial and coronal planes, respectively.

Discussion

The success of modern RT has been largely technology driven. An alternate route forward is to leverage current precise technologies and pursue biology-driven enhancements. The preclinical setting is ideal for such testing and therefore requires RT methodologies analogous to clinical approaches. The work presented herein will allow such preclinical IMRT treatments on pre-existing small animal irradiators in a cost-effective manner using 3D printing technology.

Dedicated preclinical RT technology is necessary; clinical technology cannot simply be applied to preclinical work due to the differences of scale (although attempts have been made[43]). The novel methodology presented for preclinical IMRT using inverse planning and 3D-printed beam compensators for modulation is one of the first full implementations of precision IMRT on the preclinical scale. Similar approaches have been proposed on the clinical scale.[44] Reverse translation of IMRT from clinical to preclinical scale (1–2 orders of magnitude smaller) has been challenging due to technical limitations in engineering appropriately small MLCs. The feasibility of modulating dose on the millimeter scale was shown using 2D planar dose optimization.[19] Many of the initial proposed approaches involved pencil-beam rastering to dose paint voxel by voxel.[19,45,46] However, these were mostly proof-of-principle studies limited to 2D dose distributions or were logistically infeasible (eg, requiring on the order of an hour per 2D dose plane with a 1-mm beam size[19] or increases in treatment time compared with unmodulated treatments by a factor of ~10 and ~100 for 2.4 mm and 1.1 mm pencil beams, respectively[46]). By contrast, for the novel approach presented herein, the entire field modulation is produced simultaneously (rather than via multiple apertures), improving efficiency because increased modulation has a less appreciable effect on treatment time (eg, compared with pencil beam rastering or variable aperture approaches). Spatial resolution limitations are primarily set by the 3D printing process and limitations in nozzle size due to the particulate nature of the metal-loaded filament.

Recently, Yoon et al[25] published a similar approach to small animal IMRT using 3D printing to create beam compensators. The fundamental difference between these approaches is that the work presented herein uses high-Z material to directly print compensators with desired attenuator thicknesses, whereas Yoon et al printed compensator molds with low-Z plastic and filled these with high-Z powder. Yoon et al discuss the potential issue of inconsistent powder settling and overfilling or overpacking of compensator mold affecting dosimetric accuracy. Our approach avoids this potential introduction of uncertainty and human error and only requires modeling of a single print material (rather than printing plastic as well as filling powder). However, the molds fabricated using more standard 3D printing plastics may have improved accuracy and reproducibility with commercial printing devices compared with compensators directly printed with the more particulate CuPLA in our work. In general, these novel uses of modern 3D printing technology represent the growing interest in developing means to implement IMRT on the preclinical scale. Furthermore, we present the first demonstration of preclinical IMRT targeting small animal tumor physiology, which is the strongest argument for the development of these novel approaches.

Aside from 3D printing approaches, to date, the only other complete system approaching clinical IMRT is the sparse orthogonal collimator (SOC) system, developed as an add-on to the XRAD225Cx and equipped with a rectangular aperture optimization inverse planning approach.[23,24] The SOC system has been shown to be extremely versatile, making use of precise motors to drive mechanical collimators for subfield shaping. Compared with the approach presented herein, the SOC system lends itself to a more automated and potentially streamlined process of treatment planning and delivery by avoiding custom printed blocks. However, SOC requires customized engineering and is currently not widely available. An advantage of the methodology presented herein is the simplicity and cost-effectiveness, with no requirement of additional specialized equipment besides an inexpensive commercially available 3D printer and printing material. Additionally, for larger and more modulated fields, delivery with a single compensated field may provide shorter treatment times.[25] Furthermore, although the presented approach is demonstrated using the XRAD225Cx platform, the technique can easily be adapted to other preclinical irradiators with either gantry or subject rotation and means of precise, isocentric localization and targeting (with appropriate beam modeling and suitable mount for fixing compensators to the irradiator for beam modulation, which could also be 3D printed). The technique therefore can have widespread application.

The utility of the 3D-printed compensator IMRT approach is demonstrated with a variety of sample plans with exceptional conformality of high dose to targets, uniform coverage of concave targets with avoidance of adjacent OARs, and SIB plans to both the hypoxic tumor core and normoxic tumor rim with sparing of surrounding normal tissue. The pability to produce preclinical SIB plans enables animal studies investigating the efficacy of targeting various biological and physiologic (eg, hypoxia) parameters while reducing confounding effects from overirradiating the entire tumor or surrounding normal tissue, as would be the case with less conformal non-IMRT approaches. In addition to SIB treatments, a useful ability of this approach is simply the delivery of a single uniform conformal dose to a target. As with clinical IMRT, this enables sparing of surrounding normal tissues, which may be less critical in animal studies but still useful when increasing tumor dose and for isolating certain radiation endpoints (eg, 3D blocks for hippocampal avoidance in rats could not meet desired dosimetric constraints and IMRT was necessary[25]). Avoidance of specific lung volumes in preclinical models can provide the opportunity to correlate directly measurable metrics (eg, animal respiratory rate, which directly measures pulmonary function) to quantify the effects of lung volume doses for eventual application in patients, and so forth. Aside from normal tissue sparing, IMRT will also help to ensure both conformality and uniformity for arbitrary targets. This is particularly important when considering standardization of how preclinical radiation doses are reported. Many studies using bulk irradiation from 1 direction report a single value for dose to target; however, due to beam attenuation, the target will receive an appreciably heterogeneous dose that may make correlating endpoints to dose challenging. This conformality and sparing of normal tissues could also help use more complex preclinical tumor models more effectively, moving from heterotopic tumor models to orthotopic or even syngeneic or spontaneous tumors.[47] Furthermore, IMRT capabilities on the preclinical scale will add value to investigations in the growing topic of the abscopal effect as well as the potential benefits of combining RT

and immunotherapy. In these contexts, preclinical studies before clinical trials can be extremely beneficial, but require sparing of neighboring organs and tissue to limit the immunosuppressive effects of RT (eg, on infiltrating dendritic cells or T cells) that may confound the effects of interest.[48–50]

Additional considerations to improve the accuracy of the technique are planned in future work. The XRAD225Cx treatment beam is a divergent and would be better matched by applying a corresponding draft angle in the compensator structure rather than using the perpendicular walls in the current model. This current approach will result in unmodeled crosstalk at isocenter, with portions of rays intersecting compensator regions corresponding to adjacent beamlets in the 2D intensity map. This blurring effect will be most exaggerated at the edges of thicker portions of the compensator and in regions further from central axis. However, based on gamma passing rates with strict spatial criteria, this is a reasonable first-order approximation for the compensator thicknesses and aperture sizes in this work. Nonetheless, future work will incorporate beam divergence into the printed compensator to avoid partial volume effects at isocenter.

Additionally, the current model does not consider beam hardening through the compensator; a single linear attenuation coefficient for the XRAD225Cx beam and the CuPLA is used to convert bixel intensities to compensator thicknesses. The beam hardening decreases the linear attenuation coefficient for increased compensator thickness, requiring even thicker compensator material to achieve the desired intensity modulation than a single attenuation coefficient will assume. Although this effect is less evident for the in-field dose distributions, resulting in the high gamma passing rates shown in the results, ignoring this factor does result in increased leakage through the compensator that is not included in the dose calculation. This is evident in Figures 5a,b and 6a,b (as well as Figs. E1 and E2), where an apparent region of low dose outside of modulated region is recorded on the exposed film, which is expected to be fully blocked in the corresponding calculated dose plane. This effect is similar to clinically underestimating MLC leakage, which results in acceptable gamma passing rates for planar dose analysis (see Figs. 5e–g and 6e–g, where this low-dose region is not included in the gamma analysis due to thresholding) but less acceptable gamma passing rates for composite dose delivered from multiple beams due to compounding unplanned low-dose contributions (see Fig. E2). For the initial model and approach used in this proof-of-concept work, additional 3D-printed WPLA field trimmers were added for composite measurements to increase the attenuation of out-of-field dose. Using a dual-extruder printer with both the CuPLA and WPLA makes this quite efficient. However, future work will investigate alternative approaches. For example, this can be accounted for within the plan optimization with a more detailed model of compensator attenuation, which will be the subject of future work. Using a parametric approach to fitting effective attenuation as a function of material thickness is being investigated.[51] A future Monte Carlo based dose calculation engine, rather than the pencil beam calculation currently used, will facilitate more rigorous consideration of effects of interactions/scatter within the compensator as well as within the treated animal and will generally improve the accuracy of the presented 3D-printed compensator-based IMRT.[52] Nevertheless, the high gamma passing rates for the individual field (without additional printed WPLA trimmers) analysis demonstrates that the main goal of using 3D-printed compensators to modulate field intensity works well. This,

combined with the excellent gamma passing rates of the composite delivery (with additional printed WPLA trimmers) as an end-to-end test of the complete methodology (multimodality image-based treatment planning, beam optimization, 3D-printed beam compensation, and isocentric precise irradiation on the preclinical scale), suggests great promise for this novel approach. Future work will continue to improve upon the logistics of handling beam hardening and other aspects not yet included in this initial proof-of-concept model.

When discussing future work, most important will be the application of this or other small animal IMRT approaches to meaningful co-clinical trials mimicking clinical trials for studying relevant radiation biology to guide personalization of RT for patients with cancer. Logistics become an important consideration in this context. Figure 8 shows a flowchart depicting the general workflow for preclinical trials of this nature, with the goal of closely mimicking the workflow for a clinical RT patient. This includes the incorporation of multimodality imaging, complex optimization-based treatment planning, and image guided delivery of each intensity modulated field. There are already commercial solutions for complex planning and delivery of small animal radiation treatments, but they have yet to incorporate the intricacies of IMRT.[53] The components of Figure 8 highlighted in yellow represent the new considerations associated with the work presented herein. Although the presented work is mainly a proof of concept and has not considered optimization of the logistics, the eventual implementation would be comparable to a previous preclinical trial treating with unmodulated fields collimated using 3D-printed apertures.[27] This preclinical trial, which essentially follows the workflow depicted in Figure 8, successfully irradiated a large number of animals (n = 54), guided by multiple imaging modalities (fused MRI, EPRI, and CT), using 3D-printed beam apertures customized for each individual animal's tumor and oxygen distribution. For that preclinical trial, MRI acquisition required ~2 hours and EPRI acquisition required ~1 hour. Animal setup and cone beam CT acquisition required ~40 minutes, while planning and treatment delivery (including 3D printing) required another ~40 minutes. Total time per animal averaged ~4.5 hours (range, 2.5–8.5 hours). Robust immobilization and multimodal image registration, as described in that work, circumvented the need for continuous anesthetization over a prolonged time. Compared with the preclinical trial methodology used in this previous work, the approach presented herein would not be expected to add significant experimental or anesthetization time. Total time per animal is expected to increase by ~30 minutes. This increase will be comprised of additional time for 3D printing (apertures require ~10 minutes each whereas IMRT compensators require ~30 minutes each), IMRT planning and optimization (currently <2 minutes, with potential acceleration as computational approach and resources improve), and treatment delivery requiring multiple gantry angles and compensator mounting (<10 additional minutes for these 5-field plans compared with 2-field plans[27]). This argues for the eventual feasibility of using 3D-printed compensators for IMRT in a preclinical trial involving a large cohort of animals. It must be noted, however, that there is a clear tradeoff in efficiency for precision with this methodology, which may only be necessary for certain preclinical trials.

The work presented is framed in the context of a problem that has plagued the field of radiation oncology for over a century: how to incorporate the known dictator of outcome, tumor hypoxia, in designing more effective cancer treatments.[31,54] The important prognostic implications of tumor hypoxia for patients with cancer have been demonstrated in vitro, in

vivo in animal models,[55,56] and to a limited extent in humans.[32–35] However, not until recently have noninvasive spatial maps of local oxygen concentration in animals been used to guide treatment with radiation.[27] Generally, it was not until IMRT was implemented clinically that the concept of a SIB to regions of disease requiring additional radiation was possible.[2] Preliminary results using EPRI oxygen images to guide SIB treatments in mice suggest that, as long suspected, there is a benefit to increasing radiation dose to hypoxic tumor regions, but that conformality in targeting hypoxic regions is crucial. Bulk tumor irradiation correlated EPRI-defined overall tumor oxygenation with treatment outcome.[55,56] More recently, spherical regions increasing dose to the hypoxic tumor region or, as a control, an equivalent spherical-shell volume of the normoxic tumor region, using circular cone apertures and arc deliveries, did not provide significant differences in tumor control, contrary to expectations. However, moving to 3D conformal treatments with 3D-printed apertures provided a necessary increase in dose conformality to see a significant difference.[27] Dose painting based on in vivo oxygen images provided by EPRI using image guided IMRT in animal models will take this further and form the basis for translating the well-known importance of tumor hypoxia as a determining factor in RT outcome into a guiding parameter for clinical radiation treatment planning. Of course, the presented methodology could have applications to studying a myriad of biologic parameters affecting radiation treatment outcome in addition to hypoxia.[47]

Conclusions

Preclinical RT technologies analogous to advanced clinical technologies are needed to facilitate more seamless translation of preclinical studies into clinical benefits for patients with cancer. This work presents a novel approach to image guided IMRT on the small animal scale using a commercially available precision preclinical irradiator, which implements inverse planning of optimized beam intensity maps that are then delivered using 3D-printed compensators. This enables spatial intensity modulation on the order of 1 mm at treatment isocenter. Planar dose analysis demonstrated impressive fidelity between planned and delivered dose distributions for a variety of complex representative treatment plans. The benefits of this approach include simple integration with existing precision small animal irradiator platforms (demonstrated here with XRAD225Cx system), the use of an extremely cost-effective approach leveraging commercially available 3D printing products, and a relatively small effect on treatment times. Although this approach was framed in the context of studying the role of hypoxia in treatment outcome, this approach will have applications to help answer a wide variety of questions regarding how to better incorporate tumor biology to improve personalization of RT treatments.

Supplementary Material

Refer to Web version on PubMed Central for supplementary material.

Acknowledgments—

The authors would like to acknowledge the invaluable administrative support from Mahmud Ghaemi and Anett Young, which facilitated this work.

This work was primarily supported by funding from the American Cancer Society IRG-16-222-56 grant via the University of Chicago Comprehensive Cancer Center (National Institutes of Health: P30 CA14599). Mouse data were acquired under IACUC protocol 71697 and with funding support from National Institutes of Health grants P41 EB002034, R01 CA098575, R50 CA211408.

References

1. Howell R Second primary cancers and cardiovascular disease after radiation therapy. NCRP report no. 170. Med Phys 2012;39:7729–7731. [PubMed: 28525099]
2. Mohan R, Wu Q, Manning M, et al. Radiobiological considerations in the design of fractionation strategies for intensity-modulated radiation therapy of head and neck cancers. Int J Radiat Oncol Biol Phys 2000; 46:619–630. [PubMed: 10701741]
3. Alfonso JC, Jagiella N, Nunez L, et al. Estimating dose painting effects in radiotherapy: A mathematical model. PLoS One 2014;9: e89380. [PubMed: 24586734]
4. Kahn J, Tofilon PJ, Camphausen K. Preclinical models in radiation oncology. Radiat Oncol 2012;7:223. [PubMed: 23270380]
5. Rosenthal N, Brown S. The mouse ascending: Perspectives for human-disease models. Nat Cell Biol 2007;9:993–999. [PubMed: 17762889]
6. Van Dyke T, Jacks T. Cancer modeling in the modern era: Progress and challenges. Cell 2002;108:135–144. [PubMed: 11832204]
7. Verhaegen F, Dubois L, Gianolini S, et al. ESTRO ACROP: Technology for precision small animal radiotherapy research: Optimal use and challenges. Radiother Oncol 2018;126:471–478. [PubMed: 29269093]
8. Hackam DG, Redelmeier DA. Translation of research evidence from animals to humans. JAMA 2006;296:1731–1732. [PubMed: 17032985]
9. Verhaegen F, van Hoof S, Granton PV, et al. A review of treatment planning for precision image-guided photon beam pre-clinical animal radiation studies. Z Med Phys 2014;24:323–334. [PubMed: 24629309]
10. Kitakabu Y, Shibamoto Y, Sasai K, et al. Variations of the hypoxic fraction in the SCC VII tumors after single dose and during fractionated radiation therapy: Assessment without anesthesia or physical restraint of mice. Int J Radiat Oncol Biol Phys 1991;20:709–714. [PubMed: 2004947]
11. Desrosiers M, DeWerd L, Deye J, et al. The importance of dosimetry standardization in radiobiology. J Res Natl Inst Stand Technol 2013; 118:403–418. [PubMed: 26401441]
12. Yoshizumi T, Brady SL, Robbins ME, et al. Specific issues in small animal dosimetry and irradiator calibration. Int J Radiat Biol 2011;87: 1001–1010. [PubMed: 21961967]
13. Clarkson R, Lindsay PE, Ansell S, et al. Characterization of image quality and image-guidance performance of a preclinical microirradiator. Med Phys 2011;38:845–856. [PubMed: 21452722]
14. Wong J, Armour E, Kazanzides P, et al. High-resolution, small animal radiation research platform with x-ray tomographic guidance capabilities. Int J Radiat Oncol Biol Phys 2008;71:1591–1599. [PubMed: 18640502]
15. Verhaegen F, Granton P, Tryggestad E. Small animal radiotherapy research platforms. Phys Med Biol 2011;56:R55–R83. [PubMed: 21617291]
16. Graves EE, Zhou H, Chatterjee R, et al. Design and evaluation of a variable aperture collimator for conformal radiotherapy of small animals using a microct scanner. Med Phys 2007;34:4359–4367. [PubMed: 18072501]
17. Zhou H, Rodriguez M, van den Haak F, et al. Development of a micro-computed tomography-based image-guided conformal radiotherapy system for small animals. Int J Radiat Oncol Biol Phys 2010;78:297–305. [PubMed: 20395069]
18. Prajapati S, Cox B, Cadman P, et al. We-e-108–07: Design of open-source binary micro mlc for small animal radiotherapy: An OSMD initiative. Med Phys 2013;40:489.
19. Stewart JM, Lindsay PE, Jaffray DA. Two-dimensional inverse planning and delivery with a preclinical image guided microirradiator. Med Phys 2013;40:101709. [PubMed: 24089899]
20. Cao G, Burk LM, Lee YZ, et al. Prospective-gated cardiac micro-ct imaging of free-breathing mice using carbon nanotube field emission x-ray. Med Phys 2010;37:5306–5312. [PubMed: 21089765]

21. Cao G, Lee YZ, Peng R, et al. A dynamic micro-ct scanner based on a carbon nanotube field emission x-ray source. Phys Med Biol 2009;54: 2323–2340. [PubMed: 19321922]
22. Wang S, Liu Z, Sultana S, et al. A novel high resolution micro-radiotherapy system for small animal irradiation for cancer research. Biofactors 2007;30:265–270. [PubMed: 18607076]
23. Woods K, Nguyen D, Neph R, et al. A sparse orthogonal collimator for small animal intensity-modulated radiation therapy part I: Planning system development and commissioning. Med Phys 2019;46:5703–5713. [PubMed: 31621920]
24. Woods K, Neph R, Nguyen D, et al. A sparse orthogonal collimator for small animal intensity-modulated radiation therapy. Part II: Hardware development and commissioning. Med Phys 2019;46:5733–5747. [PubMed: 31621091]
25. Yoon SW, Kodra J, Miles DA, et al. A method for generating intensity modulated radiation therapy fields for small animal irradiators utilizing 3d printed compensator molds. Med Phys 2020;47: 4363–4371. [PubMed: 32281657]
26. Ezzell GA, Burmeister JW, Dogan N, et al. Imrt commissioning: Multiple institution planning and dosimetry comparisons, a report from AAPM task group 119. Med Phys 2009;36:5359–5373. [PubMed: 19994544]
27. Epel B, Maggio MC, Barth ED, et al. Oxygen-guided radiation therapy. Int J Radiat Oncol Biol Phys 2019;103:977–984. [PubMed: 30414912]
28. Epel B, Redler G, Halpern HJ. How in vivo epr measures and images oxygen. Adv Exp Med Biol 2014;812:113–119. [PubMed: 24729222]
29. Epel B, Redler G, Pelizzari C, et al. Approaching oxygen-guided intensity-modulated radiation therapy. Adv Exp Med Biol 2016;876: 185–193. [PubMed: 26782211]
30. Epel B, Redler G, Tormyshev V, et al. Towards human oxygen images with electron paramagnetic resonance imaging. Adv Exp Med Biol 2016;876:363–369. [PubMed: 26782233]
31. Schwartz G Ueber desensibilisierung gegen rontgen und radiumstrahlen. Munchener Medizinische Wochenschrift 1909;24:1–2.
32. Hockel M, Knoop C, Schlenger K, et al. Intratumoral po2 predicts survival in advanced cancer of the uterine cervix. Radiother Oncol 1993;26:45–50. [PubMed: 8438086]
33. Hockel M, Schlenger K, Aral B, et al. Association between tumor hypoxia and malignant progression in advanced cancer of the uterine cervix. Cancer Res 1996;56:4509–4515. [PubMed: 8813149]
34. Hockel M, Schlenger K, Hockel S, et al. Tumor hypoxia in pelvic recurrences of cervical cancer. Int J Cancer 1998;79:365–369. [PubMed: 9699528]
35. Kolstad P Intercapillary distance, oxygen tension and local recurrence in cervix cancer. Scand J Clin Lab Invest Suppl 1968;106: 145–157. [PubMed: 5731701]
36. Wieser HP, Cisternas E, Wahl N, et al. Development of the open-source dose calculation and optimization toolkit matrad. Med Phys 2017;44:2556–2568. [PubMed: 28370020]
37. Bortfeld T, Schlegel W, Rhein B. Decomposition of pencil beam kernels for fast dose calculations in three-dimensional treatment planning. Med Phys 1993;20:311–318. [PubMed: 8497215]
38. Walters BKI, Rogers DWO. Dosxyznrc users manual. NRCC Report PIRS-794(revB) 2011.
39. Lindsay PE, Granton PV, Gasparini A, et al. Multi-institutional dosimetric and geometric commissioning of image-guided small animal irradiators. Med Phys 2014;41:031714. [PubMed: 24593718]
40. Morrison H, Menon G, Sloboda RS. Radiochromic film calibration for low-energy seed brachytherapy dose measurement. Med Phys 2014; 41:072101. [PubMed: 24989396]
41. Low DA, Harms WB, Mutic S, et al. A technique for the quantitative evaluation of dose distributions. Med Phys 1998;25:656–661. [PubMed: 9608475]
42. Gonet M, Epel B, Halpern HJ, et al. Merging preclinical EPR tomography with other imaging techniques. Cell Biochem Biophys 2019; 77:187–196. [PubMed: 31440878]
43. Parsons D, Church C, Syme A. Toward a pre-clinical irradiator using clinical infrastructure. Phys Med 2019;58:21–31. [PubMed: 30824146]
44. Avelino SR, Silva LF, Miosso CJ. Use of 3d-printers to create intensity-modulated radiotherapy compensator blocks. Conf Proc IEEE Eng Med Biol Soc 2012;2012:5718–5721.

45. Cho N, Wong J, Kazanzides P. Dose painting with a variable collimator for the small animal radiation research platform (SARRP). MICCAI Workshop on Image-Guided Adaptive Radiation Therapy (IGART). Boston, MA; 2014. Available at: http://hdl.handle.net/10380/3476. Accessed January 19, 2021.
46. van Hoof SJ, Verde JB, Verhaegen F. Dose painting by dynamic irradiation delivery on an image-guided small animal radiotherapy platform. Br J Radiol 2019;92:20180744. [PubMed: 30706718]
47. Day CP, Merlino G, Van Dyke T. Preclinical mouse cancer models: A maze of opportunities and challenges. Cell 2015;163:39–53. [PubMed: 26406370]
48. Siva S, MacManus MP, Martin RF, et al. Abscopal effects of radiation therapy: A clinical review for the radiobiologist. Cancer Lett 2015; 356:82–90. [PubMed: 24125863]
49. Weichselbaum RR, Liang H, Deng L, et al. Radiotherapy and immunotherapy: A beneficial liaison? Nat Rev Clin Oncol 2017;14: 365–379. [PubMed: 28094262]
50. Ngwa W, Irabor OC, Schoenfeld JD, et al. Using immunotherapy to boost the abscopal effect. Nat Rev Cancer 2018;18:313–322. [PubMed: 29449659]
51. Chang SX, Cullip TJ, Deschesne KM, et al. Compensators: An alternative IMRT delivery technique. J Appl Clin Med Phys 2004;5: 15–36.
52. Brualla L, Rodriguez M, Lallena AM. Monte carlo systems used for treatment planning and dose verification. Strahlenther Onkol 2017; 193:243–259. [PubMed: 27888282]
53. van Hoof SJ, Granton PV, Verhaegen F. Development and validation of a treatment planning system for small animal radiotherapy: Smart-plan. Radiother Oncol 2013;109:361–366. [PubMed: 24183860]
54. Salem A, Asselin MC, Reymen B, et al. Targeting hypoxia to improve non-small cell lung cancer outcome. J Natl Cancer Inst 2018; 110.
55. Elas M, Bell R, Hleihel D, et al. Electron paramagnetic resonance oxygen image hypoxic fraction plus radiation dose strongly correlates with tumor cure in FSA fibrosarcomas. Int J Radiat Oncol Biol Phys 2008;71:542–549. [PubMed: 18474313]
56. Elas M, Magwood JM, Butler B, et al. EPR oxygen images predict tumor control by a 50% tumor control radiation dose. Cancer Res 2013;73:5328–5335. [PubMed: 23861469]

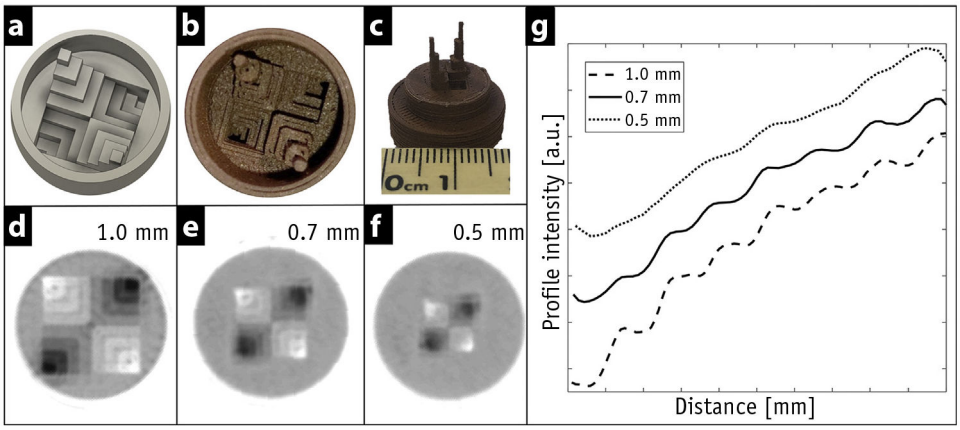

Fig. 1.

In-plane spatial resolution test patterns to determine bixel size limitations. (a) Three-dimensional (3D) model of pyramidal step function pattern with discrete step widths of 0.5, 0.7, or 1.0 mm (displayed). Copper-doped polylactic acid (CuPLA) 3D-printed 1.0-mm test pattern (b) from beam's-eye perspective and (c) showing internal features viewed from the side. Radiographs (d-f) of printed test patterns (variable grayscale intensity corresponds to variable thickness) and (g) profiles across these images (offset vertically for visualization) showing degradation of printed features smaller than 0.7 mm.

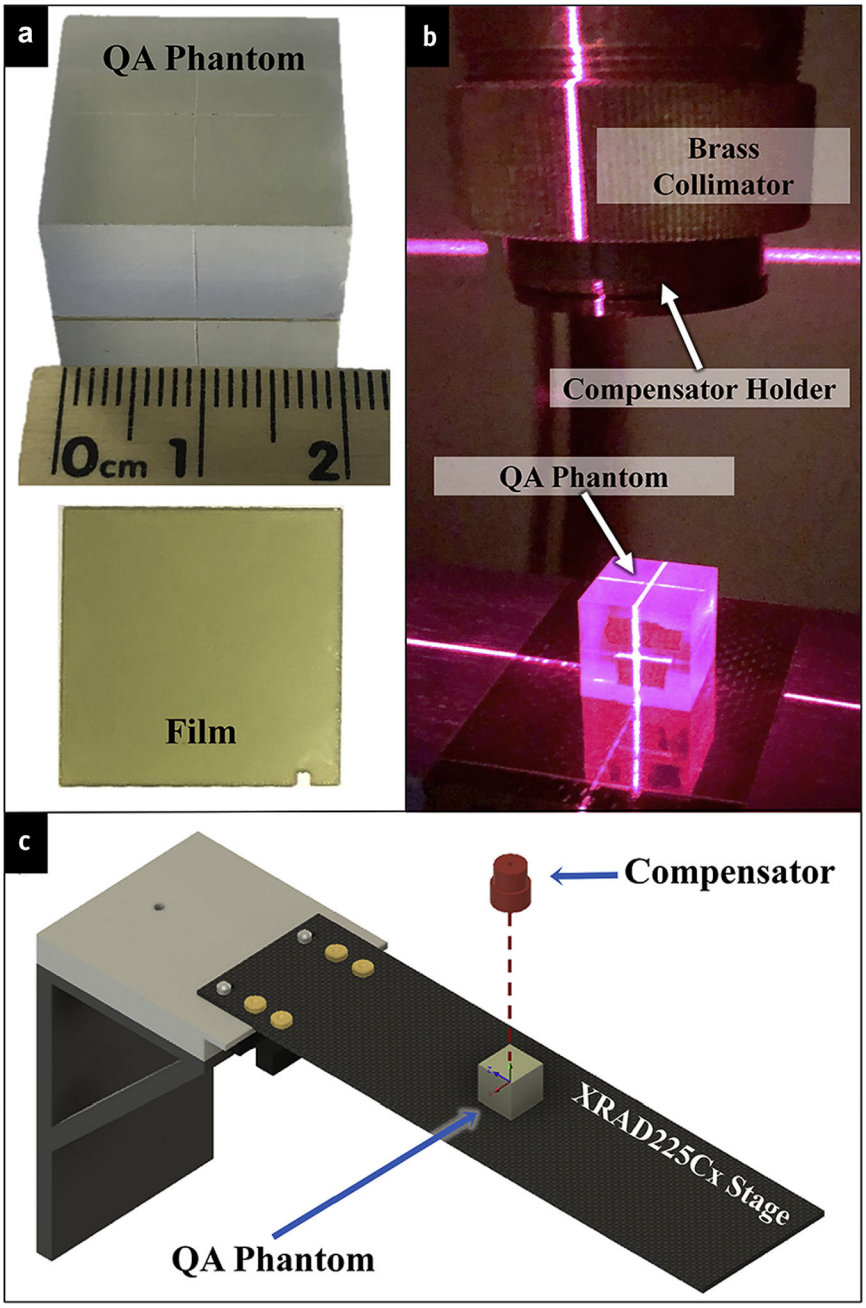

Fig. 2.

(a) Acrylic 20 × 20 × 20 mm^3 quality assurance (QA) phantom holding gafchromic film (20 × 20 mm^2) shown below phantom. (b) Laser-guidance system used with cone beam computed tomography (CBCT) for alignment as well as brass collimator and compensator holder. (c) Three-dimensional (3D) model of XRAD225Cx stage with QA phantom and compensator (at gantry 0°).

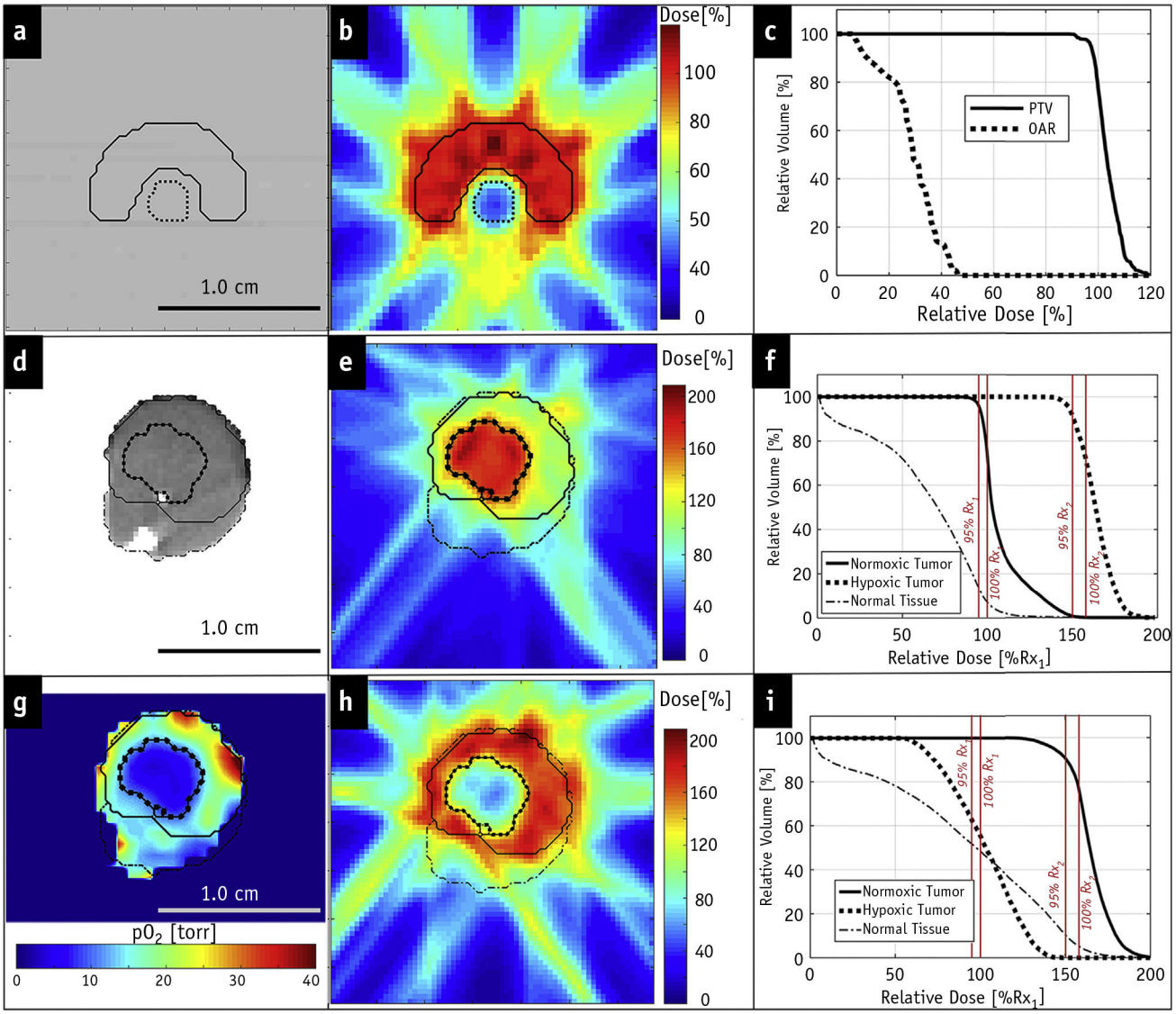

Fig. 3.

Data from intensity modulated radiation therapy (IMRT) plans for the miniaturized American Association of Physicists in Medicine TG119 C-shape target (first row), electron paramagnetic resonance imaging (EPRI)-guided hypoxic boost (second row), and inverted boost (third row). Planned dose distributions in the plane of gantry rotation are shown in the second column. Associated dose-volume histograms (DVHs) are shown in the third column. (a) Computed tomography (CT) slice in plane of gantry rotation showing planning target volume (PTV) (solid line) and organs at risk (OARs) (dotted line) for the TG119 C-shape plan. (d) CT slice of tumor-bearing mouse leg in plane of gantry rotation showing hypoxic tumor (dash line), entire tumor (solid line), and mouse leg (dotted-dashed line). (g) EPRI oxygen image in plane of gantry rotation. Doses for mouse tumor simultaneous integrated boost (SIB) oxygen-based dose painting are normalized to Rx_1 (vertical red lines highlighting doses of interest: 100% and 95% of both Rx_1 & Rx_2).

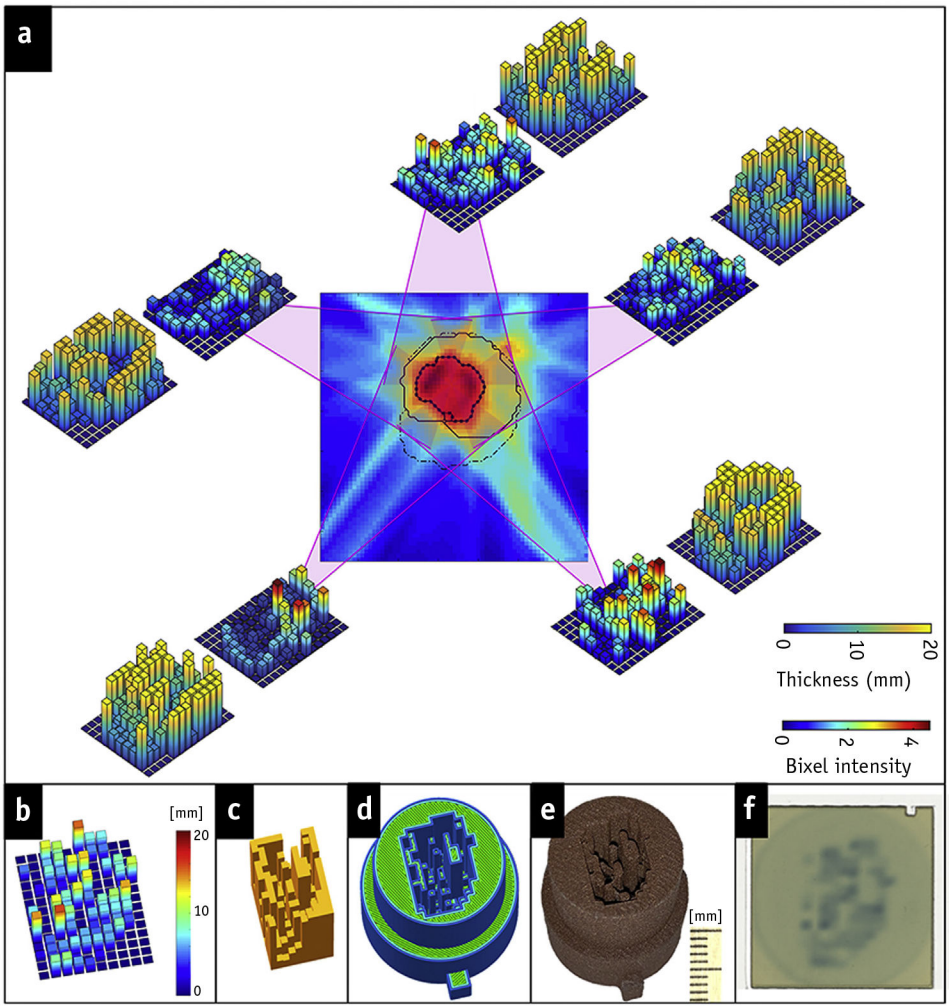

Fig. 4.

Depiction of proposed preclinical intensity modulated radiation therapy (IMRT) methodology. (a) Optimization of bixel intensities (inner 2-dimensional [2D] maps) from different gantry angles to produce desired 3-dimensional (3D) dose distribution (central image), which are converted into compensator thickness (outer 2D maps) to modulate beams and produce desired intensities. For 1 specific beam, (b-f) depict the intensity map, corresponding compensator thickness map, conversion to 3D printer file within compensator plug, compensator printed using copper-doped polylactic acid (CuPLA), and modulated beam intensity delivered to film, respectively.

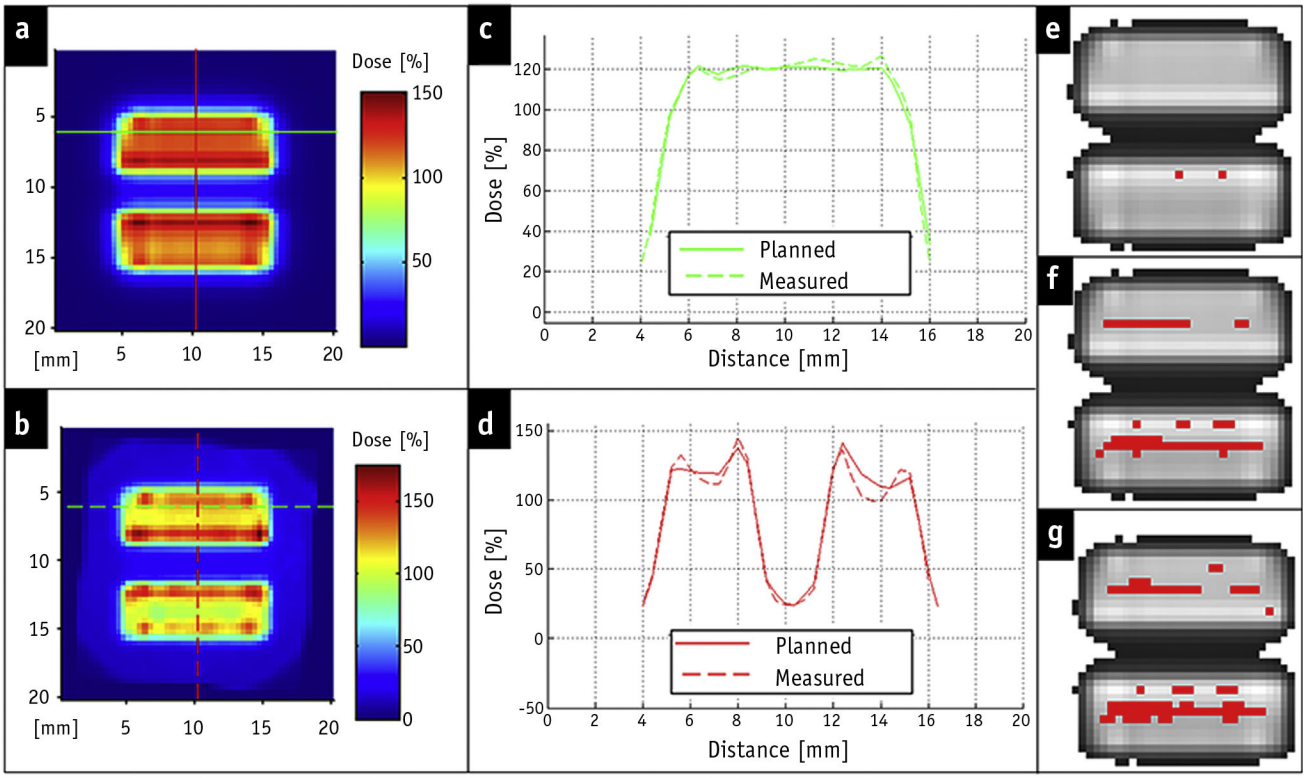

Fig. 5.

One of 5 intensity modulated radiation therapy (IMRT) fields (gantry = 0°) from miniaturized C-shape plan delivered to film within quality assurance (QA) phantom. (a) Planned and (b) delivered dose. (c) Horizontal and (d) vertical dose profiles corresponding to lines shown in (a) and (b). Gamma analysis results are overlaid on planned dose (grayscale) with thresholded (<15% max dose) points removed and failing points in red for criteria of (e) 3%/1.0 mm, (f) 3%/0.7 mm, and (g) 3%/0.5 mm.

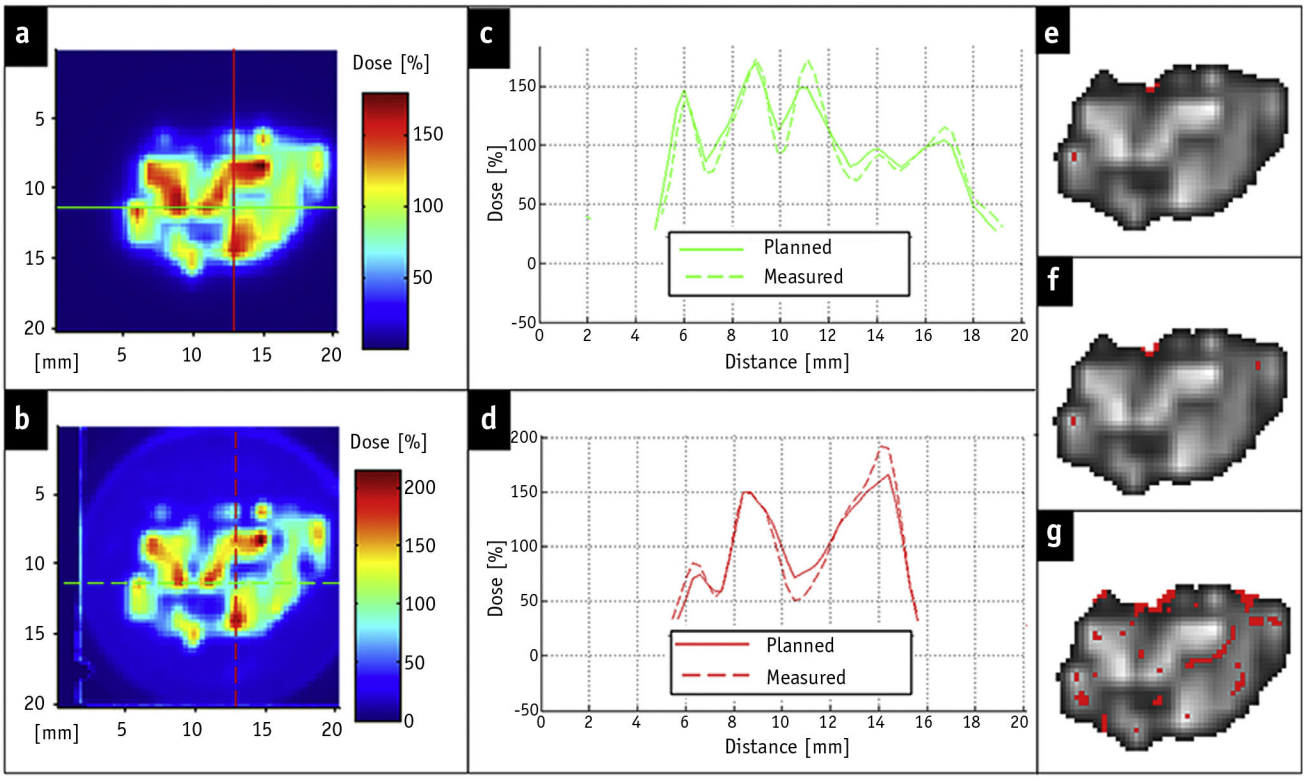

Fig. 6.

One of 5 intensity modulated radiation therapy (IMRT) fields (gantry = 0°) from electron paramagnetic resonance imaging (EPRI)-guided hypoxia-boost delivered to film within quality assurance (QA) phantom. (a) Planned and (b) delivered dose. (c) Horizontal and (d) vertical dose profiles corresponding to lines shown in (a) and (b). Gamma analysis results displayed overlayed on planned dose (grayscale) with thresholded (<15% max dose) points removed and failing points in red for (e) 3%/1.0 mm, (f) 3%/0.7 mm, and (g) 3%/0.5 mm.

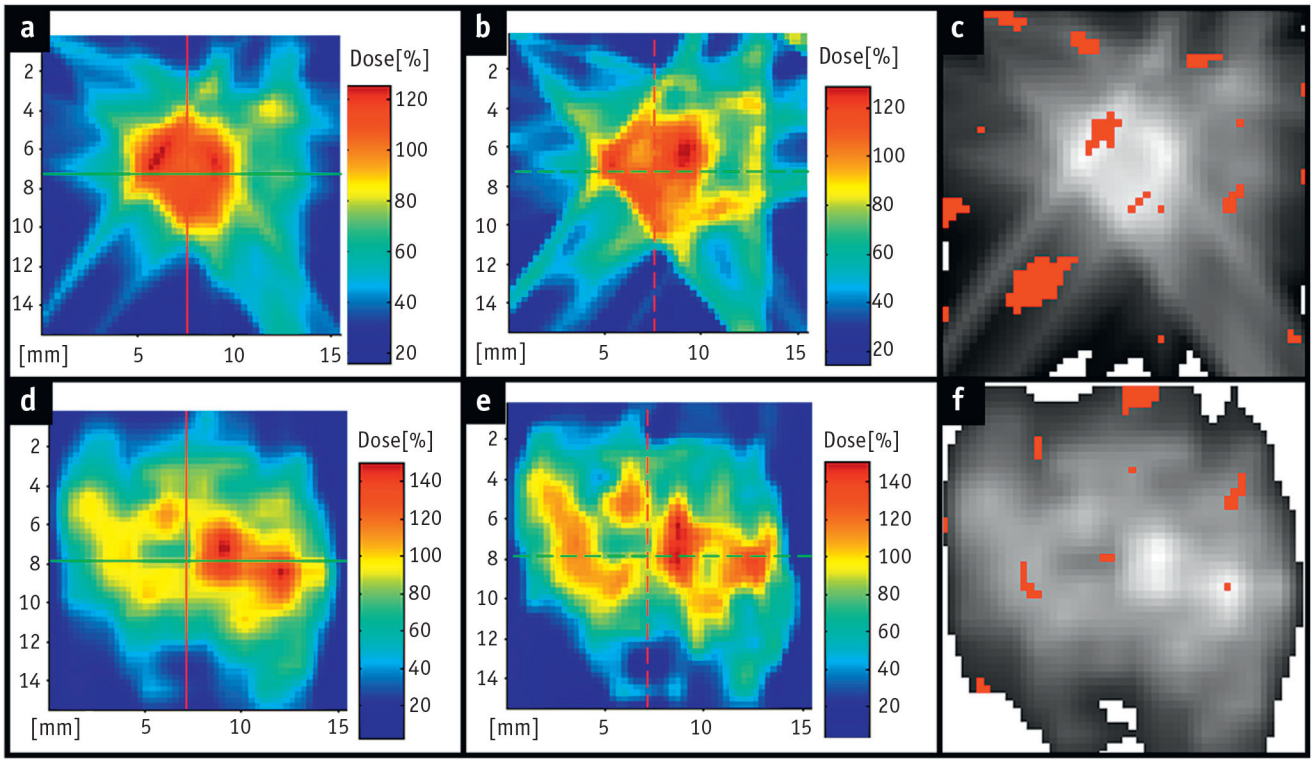

Fig. 7.

Flow chart depicting general approach to a preclinical image guided intensity modulated radiation therapy (IMRT) treatment workflow, which is analogous to that of a clinical radiation therapy patient. Yellow components highlight modifications specific to the 3-dimensional (3D) printed compensator-based IMRT presented in this work. Tasks are categorized as follows: Rectangle = imaging; oval = manual intervention required; hexagon = computer input required; diamond = automated.

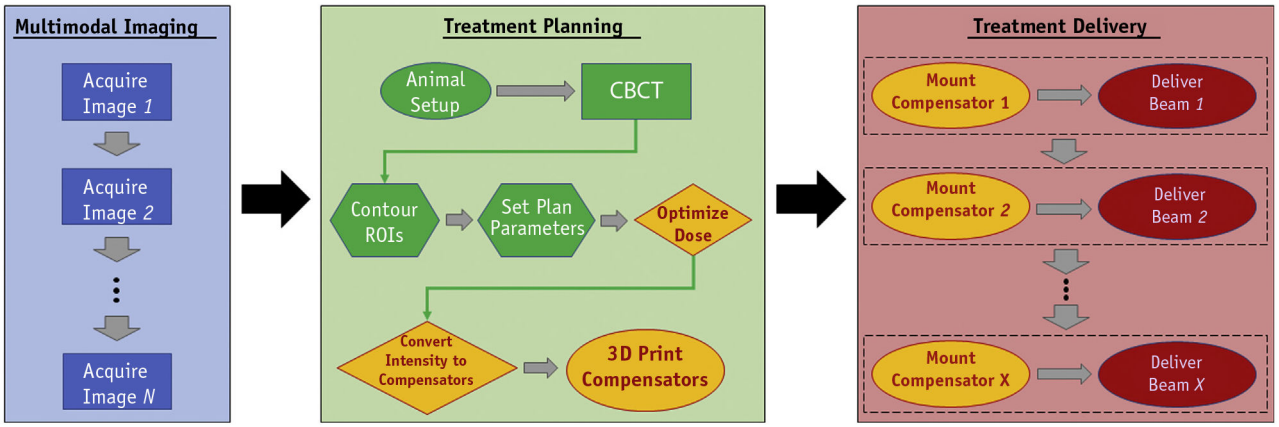

Fig. 8.

Composite dose distribution from end-to-end test delivering all 5 intensity modulated radiation therapy (IMRT) fields for the hypoxia boost plan to the quality assurance (QA) phantom. The top row shows the central axial slice (plane of gantry rotation) and the bottom row shows the central coronal slice (plane orthogonal to 0° beam axis). Planned dose distributions are in (a) and (d) and measured dose distributions are in (b) and (e) for axial and coronal planes, respectively. Gamma analysis results overlaid on planned dose (grayscale) with thresholded (<15% max dose) points removed and failing points in red for criterion of 3%/1.0 mm shown in (c) and (f) for axial (95.3% pass) and coronal (98.1% pass) planes, respectively.